Supplement of Atmos. Meas. Tech., 15, 561–572, 2022
https://doi.org/10.5194/amt-15-561-2022-supplement

Atmospheric Measurement Techniques
Open Access
EGU

Supplement of

Comparing black-carbon- and aerosol-absorption-measuring instruments – a new system using lab-generated soot coated with controlled amounts of secondary organic matter

Daniel M. Kalbermatter et al.

Correspondence to: Konstantina Vasilatou (konstantina.vasilatou@metas.ch)

S1 Operation points of miniCAST generator and OCU

Table S1 provides the operation points used for both the miniCAST generator and the OCU. The overall C/O ratio is calculated as (Schnaiter et al., 2006)[1]

$$\mathrm{C/O} = 7.16\ \frac{f_\mathrm{f}}{f_\mathrm{air}} \quad \text{(S1)}$$

where f_f is the flow of propane fuel and the f_air the flow of air (oxidation air + mixing air).

Mass concentrations of α-pinene are regulated by indicating the setpoint for the PID response in mV. Those values are converted to molar ratio (ppm) using the results of the regular calibrations with a 100-ppm isobutylene–air mixture as well as the response factor for α-pinene reported by the manufacturer (0.34). From the molar ratio the mass concentration was calculated using the ideal gas law.

[1]Schnaiter, M., Gimmler, M., Llamas, I., Linke, C., Jäger, C., and Mutschke, H.: Strong spectral dependence of light absorption by organic carbon particles formed by propane combustion, Atmos. Chem. Phys., 6, 2981–2990, https://doi.org/10.5194/acp-6-2981-2006, 2006.

Table S1: Operation points of the miniCAST 5201 Type BC generator and the OCU used in this study.

miniCAST 5201 Type BC						
Operation point	**Propane (mL min^{-1})**	**Oxidation air (L min^{-1})**	**Mixing air (mL min^{-1})**	**Quench gas N_2 (L min^{-1})**	**Dilution air (L min^{-1})**	**Overall C/O ratio (-)**
1	60	1.1	350	7	10	0.296
0.1	60	1.3	220	7	10	0.283

OCU				
Setup	**Operation point**	***GMD*$_{mob}$ (nm)[1]**	**α-pinene mass concentration (mg/m^3)**	**α-pinene/eBC$_{PAX}$ mass ratio**
1	1 – uncoated	91.7±0.1	0	0
1	1 – coating 1	86.1±0.1	92	11
1	1 – coating 2	83.4±0.1	282	42
1	1 – coating 3	83.0±0.1	911	140
0.1	0.1 – uncoated	88.3±0.1	0	0
0.1	0.1 – coating 1	90.2±0.1	92	78
0.1	0.1 – coating 2	111 ±1	549	414
0.1	0.1 – coating 3	126±1	732	552

[1]The uncertainties for the GMD_{mob} correspond to one standard deviation of the mean (k=1; 68 % confidence interval; number of measurements n=29–35).

In Table S1 two different operation points of the miniCAST BC are listed. For Setup 1 (i.e. no dilution unit between the miniCAST and OCU), we had to slightly modify the settings of the miniCAST in order to still generate soot with GMD_{mob} of 90 nm. Without modifying the setting, we would obtain particles with GMD_{mob} > 90 nm due to coagulation. We believe that coagulation happens already in the outlet pipe of the miniCAST (and perhaps in the tube connecting the miniCAST with the OCU). To check whether particle coagulation occurs in the OCU, we measured the particle size distribution at the inlet and outlet of the OCU with an SMPS and found no difference. We believe that no further coagulation was observed in the OFR most likely because of the short residence time of the aerosols in the quartz tube (about 3 s).

S2 Design of custom-made flow splitter

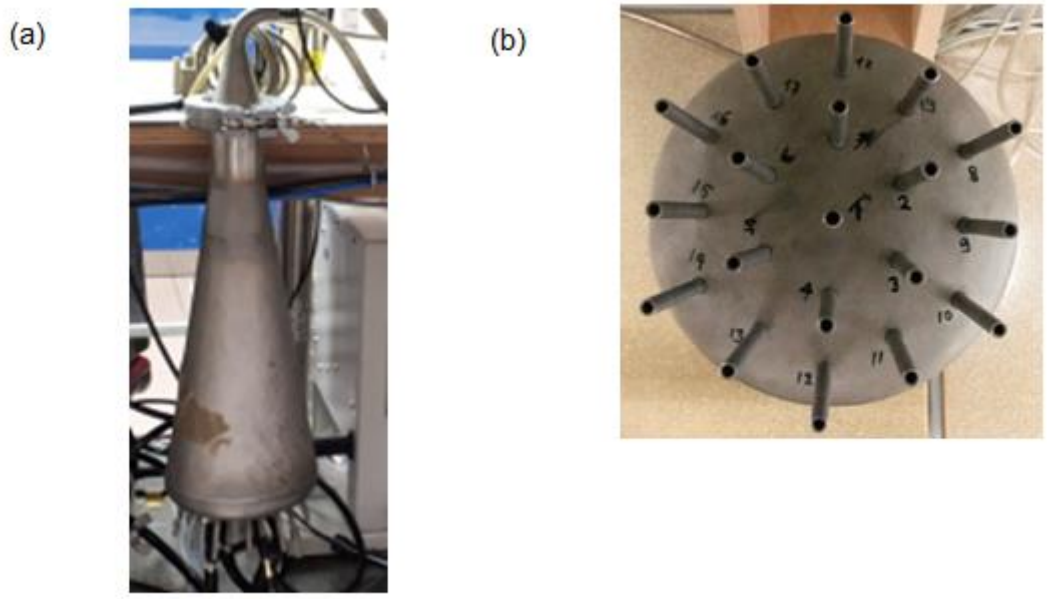

Figure S1: Picture of the custom-made flow splitter used in this study (a), which accommodates 19 equivalent sampling ports (b).

S3 Irregularities in MAAP data

While the oscillations coincide with the frequency of filter spot changes, the actual spot change takes place during a steadier period of the oscillations. Therefore, as stated in the manuscript chapter 2.2, the oscillations are not related e.g. to the spot-change related artefact described by (Hyvärinen et al., 2013).

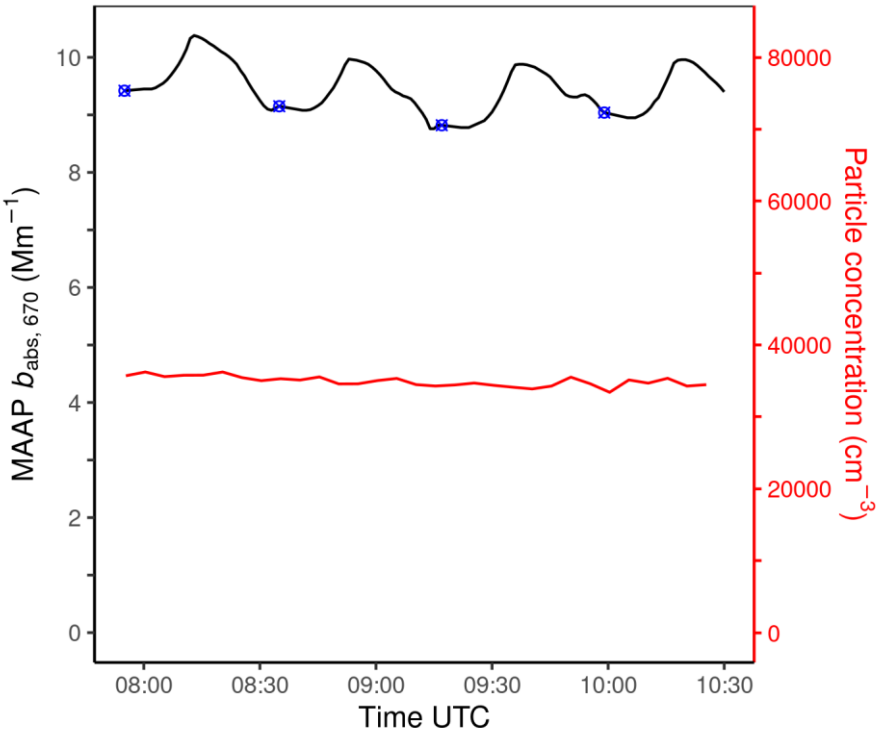

Figure S2: Example of MAAP b_{abs} data showing a periodic variation of the signal over time. This behaviour was consistently observed but was more pronounced at higher concentrations. The data shown are from the measurement of the operation point "1 – coating 1". Total number concentration as measured by SMPS is shown on the secondary y-axis. The blue squares designate the time of the filter spot changes.

S4 Description of the PAS

The measurement principle of the PAS is based on the photo-acoustic effect of light absorbing particles in an acoustic resonator, as shown in Fig. S3. BC particles in the laser beam absorb light (1), which causes them to heat up (2). This heat is transferred to the carrier gas, releasing a pressure wave from the particle (3). This effect is enhanced if the light is modulated at the right frequency (4), building a standing wave within the resonator which is measured with a sensitive microphone (5). By matching the light intensity modulation frequency with the resonance frequencies of the chamber, the quality factor of the acoustic mode (Q ~ 1000 at 22.7 kHz) enhances the signal amplitude. The amplitude corresponds linearly to the amount of absorbed light.

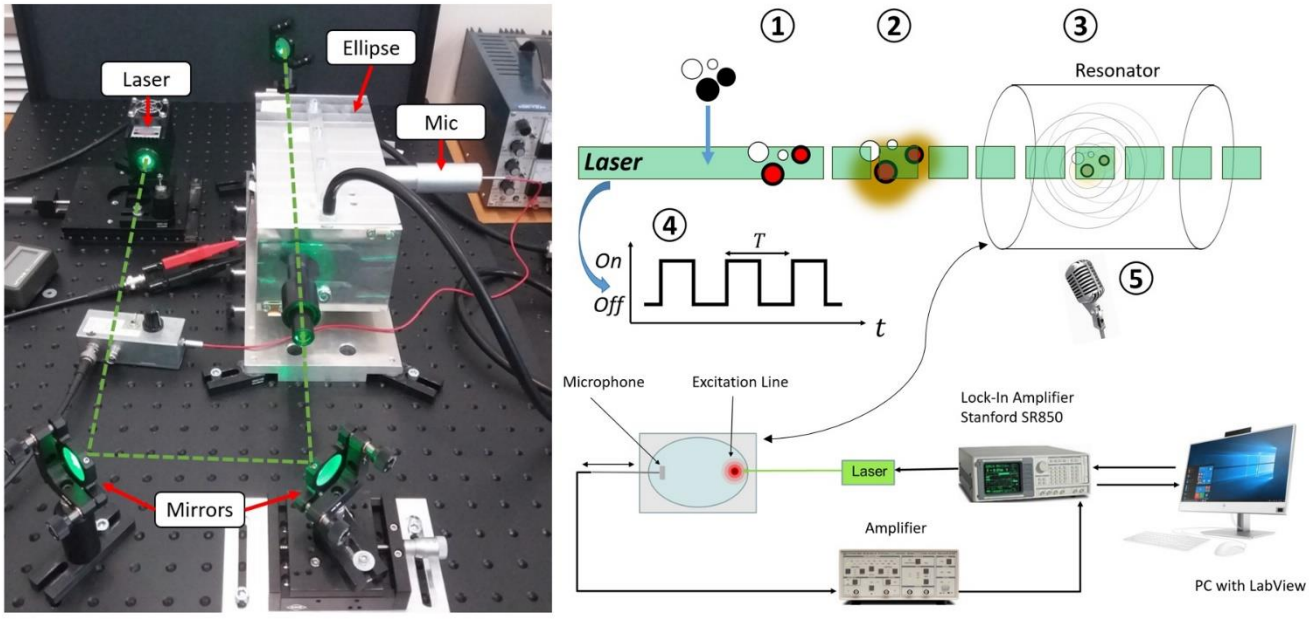

- **Figure S3. The measurement setup and schematic, and an illustration of the photoacoustic effect.**

The photoacoustic instrument uses a novel resonator chamber with elliptical cross-section (10 cm width, 8 cm height) to enhance the photoacoustic signal, three lasers, a microphone, a loudspeaker, an amplifier and a signal-processing unit (lock-in amplifier). The three different wavelengths (445 nm with 300 mW, 520 nm with 300 mW, 638 nm with 300 mW power) of the diode-lasers allow to measure wavelength-dependent optical properties of the aerosols. The laser wavelength is switched periodically every 60 seconds from blue to green to red, using only one wavelength at a given time. The three laser beam paths were combined inside the laser housing by way of dichroic mirrors.

The motivation for the elliptical cross-section is the possibility to separate the excitation position from the measurement position of the microphone - at approximately the two focal points of the ellipse. The laser beam is guided by mirrors into the

aluminium resonator along a focal cylinder, which allows effective excitation of the transversal modes. The loudspeaker and the microphone are both guided with the help of a rod into the resonator chamber and are sealed to ensure a leak-free chamber. The microphone, Knowles SPU1410LR5H-QB, is situated in the mid of the 24 cm long resonator case and can be moved transversally into the resonator, as indicated in Fig. S3. The microphone signal is then amplified and demodulated with a Stanford SR850 lock-in amplifier, which allows to measure the amplitude and phase of the photoacoustic signal at the excitation frequency, of around 22.7 kHz. The measurements were performed with an integration time of 1 second allowing full build up of a standing wave. Aerosols enter at one end of the resonator, and are drawn out at the other end using a pump. Response times to sudden aerosol inputs were in the order of three to four minutes. The laser intensity modulation frequency is adapted periodically every 10 minutes, with the help of a loudspeaker and a frequency sweep, to match the resonance frequency of the chamber.

A loudspeaker (not shown in Fig. S3), Balanced Armature Driver WBFK-30095-000, is guided into the ellipse (parallel to the microphone) and excites the acoustic modes of the resonator chamber. The acoustic modes are independent of the light-absorbing particles in the chamber, but depend on the gas composition, temperature and pressure. The frequency of the loudspeaker is swept within a window where an acoustic resonance occurs. The frequency of the amplitude peak of this spectrum is then determined and its relative shift (compared to a reference measurement) is added to the laser intensity modulation frequency.

The motivation for the use of a higher than standard frequency is the larger Q factors that we measured for the higher order modes. Also, measurements in the ultrasonic regime are expected to be less influenced by ambient acoustic noise.

S5 Data tables

Table S2: b_{abs} converted to 532 nm. The uncertainties correspond to one standard deviation of the mean (k=1; 68 % confidence interval; number of measurements n =100–180).

Operation point	R_{BC} (-)	$b_{abs,\,532}$ (Mm^{-1})					
		AE33 (520 nm)	MSPTI (532 nm)	PAX (870 nm)	MAAP (637 nm)	PAS (520 nm)	PTAAM (532 nm)
1 - uncoated	0	107.6±0.3	39.0±0.6	42.8±0.3	64.0±0.3	42.2±2.0	49.8±0.2
1 - coating 1	0.47±0.02	102.4±0.2	52.4±0.5	42.6±0.1	57.9±0.2	70.5±0.9	49.8±0.1
1 - coating 2	0.83±0.02	113.8±0.2	51.5±0.3	41.6±0.1	59.1±0.2	54.1±0.5	47.4±0.1
1 - coating 3	0.87±0.02	116.3±0.3	47.2±0.4	40.2±0.1	59.0±0.2	74.1±1.0	46.7±0.1
0.1 - uncoated	0	107.6±0.7	40.1±0.9	46.0±0.3	62.5±0.3	33.1±0.5	52.5±0.2
0.1 - coating 1	1.42±0.02	140.9±0.3	51.8±0.4	52.0±0.3	78.3±0.4	90.5±0.8	57.8±0.2
0.1 - coating 2	1.95±0.02	159.5±0.5	50.4±0.6	54.7±0.2	95.7±0.5	48.7±0.6	62.0±0.2

0.1 - coating 3	3.36±0.07	176.1±1.3	78.4±0.7	59.5±0.4	125±1	36.0±0.8	68.7±0.2

Table S3: E_{babs} at 532 nm. The uncertainties correspond to one standard deviation of the mean (k=1; 68 % confidence interval; n=100–180).

Operation point	R_{BC} (-)	$E_{babs,\,532}$ (-)					
		AE33 (520 nn)	MSPTI (532 nm)	PAX (870 nm)	MAAP (637 nm)	PAS (520 nm)	PTAAM (532 nm)
1 - uncoated	0	1.00±0.01	1.00±0.02	1.00±0.01	1.00±0.01	1.00±0.07	1.00±0.01
1 - coating 1	0.47±0.02	0.952±0.004	1.35±0.02	0.997±0.007	0.905±0.005	1.67±0.08	1.00±0.01
1 - coating 2	0.83±0.02	1.06±0.01	1.32±0.02	0.972±0.007	0.924±0.005	1.29±0.06	0.953±0.004
1 - coating 3	0.87±0.02	1.08±0.01	1.21±0.02	0.939±0.007	0.921±0.005	1.77±0.09	0.939±0.004
0.1 - uncoated	0	1.00±0.01	1.00±0.03	1.00±0.01	1.00±0.01	1.00±0.02	1.00±0.01
0.1 - coating 1	1.42±0.02	1.31±0.01	1.29±0.03	1.13±0.01	1.25±0.01	2.72±0.05	1.10±0.01
0.1 - coating 2	1.95±0.02	1.49±0.01	1.26±0.03	1.19±0.01	1.53±0.01	1.47±0.03	1.18±0.01
0.1 - coating 3	3.36±0.07	1.64±0.02	1.96±0.05	1.29±0.01	2.00±0.02	1.08±0.03	1.31±0.01

Table S4: b_{abs} and E_{babs} at 950 nm calculated from the measurements taken by the instruments used in this study. The uncertainties correspond to one standard deviation of the mean (k=1; 68 % confidence interval; n=100–160).

Operation point	R_{BC} (-)	$b_{abs,\,950}$ (Mm^{-1})			$E_{babs,\,950}$ (-)		
		AE33 (950 nm)	PAX (870 nm)	PTAAM (1064 nm)	AE33 (950 nm)	PAX (870 nm)	PTAAM (1064 nm)
0.1 - uncoated	0.0±0.1	74.0±0.5	28.7±0.1	31.8±0.4	1.00±0.01	1.00±0.01	1.00±0.02
0.1 - coating 1	1.4±0.1	94.4±0.3	27.6±0.1	28.8±0.3	1.28±0.01	0.963±0.005	0.90±0.02
0.1 - coating 2	2.0±0.1	99.3±0.4	27.2±0.1	28.8±0.2	1.34±0.01	0.948±0.004	0.91±0.01
0.1 - coating 3	3.4±0.4	111±1	27.5±0.1	31.1±0.4	1.50±0.02	0.959±0.005	0.98±0.02

S6. Stability of the PTAAM-2λ response during AEROTOX campaign

Instrument performance was tested every working day during the campaign (Figure S4). The response of channel 1 was determined by measuring the absorption of 1 ppm NO_2. The response of channel 2 was determined by multiplying the response of channel 1 with the absorption ratio ($b_{abs,\,ch2}/b_{abs,\,ch1}$) obtained for aerosolized nigrosin.

The standard deviation of the instrument response was 3 % for channel 1 and 4 % for channel 2.

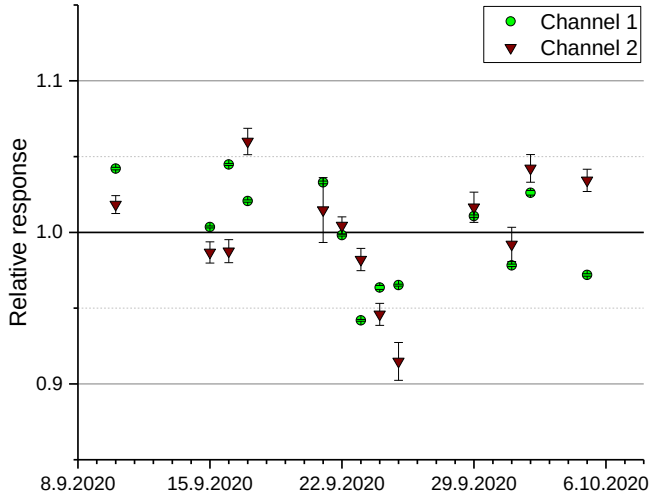

Figure S4. Relative response of PTAAM-2λ during the campaign. Error bars represent one standard deviation of the mean.

S7 Comparison of MSPTI and PTAAM

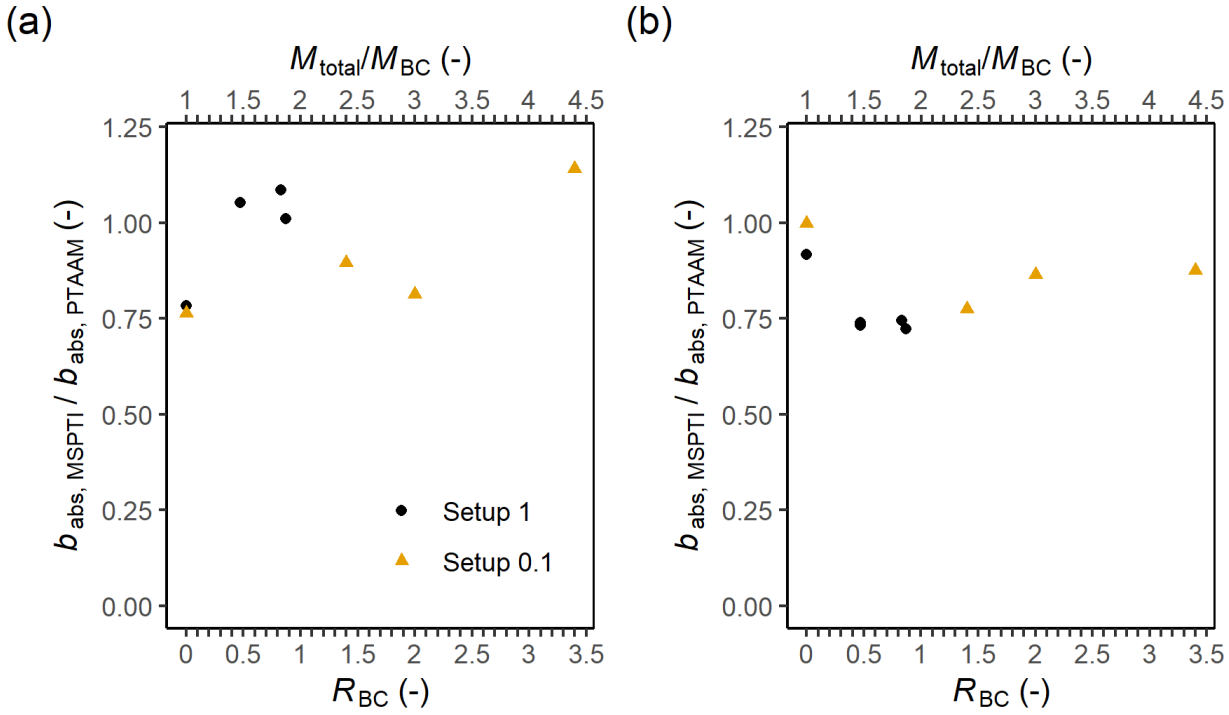

Figure S5. Absorption ratio MSPTI/PTAAM measured at 532 nm as a function of total mass to BC mass ratio and R_{BC} during the main experiments (a) and the additional experiments (b).